catalysts

MDPI

Article

$BaTi_{0.8}B_{0.2}O_3$ (B = Mn, Fe, Co, Cu) LNT Catalysts: Effect of Partial Ti Substitution on NOx Storage Capacity

Craig Aldridge, Verónica Torregrosa-Rivero, Vicente Albaladejo-Fuentes, María-Salvadora Sánchez-Adsuar and María-José Illán-Gómez *

Departamento de Química Inorgánica, Facultad de Ciencias, Universidad de Alicante, Ap. 99, E-03080 Alicante, Spain; craigald@hotmail.co.uk (C.A.); vero.torregrosa@ua.es (V.T.-R.); vicentealbaladejo@gmail.com (V.A.-F.); dori@ua.es (M.-S.S.-A.)

* Correspondence: illan@ua.es; Tel.: +34-965903975

Received: 6 March 2019; Accepted: 16 April 2019; Published: 18 April 2019

Abstract: The effect of partial Ti substitution by Mn, Fe, Co, or Cu on the NOx storage capacity (NSC) of a $BaTi_{0.8}B_{0.2}O_3$ lean NOx trap (LNT) catalyst has been analyzed. The $BaTi_{0.8}B_{0.2}O_3$ catalysts were prepared using the Pechini's sol–gel method for aqueous media. The characterization of the catalysts (BET, ICP-OES, XRD and XPS) reveals that: i) the partial substitution of Ti by Mn, Co, or Fe changes the perovskite structure from tetragonal to cubic, whilst Cu distorts the raw tetragonal structure and promotes the segregation of Ba_2TiO_4 (which is an active phase for NOx storage) as a minority phase and ii) the amount of oxygen vacancies increases after partial Ti substitution, with the $BaTi_{0.8}Cu_{0.2}O_3$ catalyst featuring the largest amount. The $BaTi_{0.8}Cu_{0.2}O_3$ catalyst shows the highest NSC at 400 °C, based on NOx storage cyclic tests, which is within the range of highly active noble metal-based catalysts.

Keywords: perovskite; NO to NO_2 oxidation; NOx storage capacity; LNT catalysts

1. Introduction

Diesel engines are a type of lean burn engine, operating at upper stoichiometric air-to-fuel ratios (A/F>14.7/1), which grew in popularity at the end of 20th century as they offered higher fuel efficiency and less CO_2 emissions respect to gasoline engines [1]. However, these engines show a highly relevant drawback since they generate large amounts of NOx and soot [2,3]. In order to minimize the level of these pollutants, more stringent standards were progressively established all over the world. Nowadays, it is accepted that the current EURO VI standard regarding NOx emissions is not met by just improving the quality of the fuel, by modifying the engine, or by using three-way-catalysts (TWCs). Consequently, alternative catalytic strategies are mandatory in order to avoid the disappearance of vehicles fitted with a diesel engine [4,5].

Two methodologies have been proposed to control NOx emission in lean burn engines: selective catalytic reduction (SCR) and NOx storage and reduction (NSR), also called lean NOx trapping (LNT). LNT technology involves the adsorption of NOx under lean conditions, followed by the periodic regeneration of the catalyst by reduction under rich conditions [6]. The conventional LNT catalysts (fitted in diesel cars) are composed of a platinum-group metal and an alkaline or alkaline-earth oxide (BaO or K_2O) supported on a high surface area material (Al_2O_3, TiO_2, ...). It has been found that LNT technology matched with a TWC in a direct-injection spark ignition (DISI) engine can feature interesting results for NOx control emission [7].

Nevertheless, these conventional LNT catalysts present some drawbacks [8], with the high cost of noble metals (mainly Pt) being one of the most relevant. In fact, an interesting challenge has been

highlighted in a recent EU report, regarding the need to develop alternatives to the use of critical raw materials such as precious metals [9]. In this line, the potential of perovskite base catalysts is being largely illustrated in the literature for environmental applications [10–12].

In previous studies [11,12], titanium was partially substituted by copper in the $BaTiO_3$ perovskite structure, showing the resulting $BaTi_{1-x}Cu_xO_3$ perovskites a high activity for NOx storage, which was attributed to the presence of oxygen vacancies (created on the catalyst surface as a consequence of the copper incorporation into the structure) and to the segregation of some phases (mainly $BaCO_3$ and Ba_2TiO_4, but also CuO). It was also concluded that the $BaTi_{0.8}Cu_{0.2}O_3$ catalyst presents a NOx storage capacity (NSC) at 420 °C in the range of levels reported for noble metal-based catalysts (around 300 μmol/g) [13], and hence could be proposed as a potential component of high-temperature LNT systems for lean burn engines, such as gasoline direct injection engines. Moreover, in the literature, other metals such as Mn, Fe, or Co have been proposed as promising B cations in the perovskite used as catalysts for NOx and soot removal [14–16]. Thus, the aim of this paper is to determine the effect of Ti partial substitution by Mn, Fe, and Co in the NSC of the $BaTi_{0.8}B_{0.2}O_3$ LNT catalyst. The results will be analyzed with respect to the performance of the previously studied $BaTi_{0.8}Cu_{0.2}O_3$ catalyst [11,12].

2. Results and Discussion

2.1. Characterization of the Catalysts

Table 1 presents the nomenclature and the basic characterization data of the catalysts: B metal content (measured by ICP-OES), BET surface area (obtained by applying the BET equation to N_2 adsorption data) and XPS. As it can be observed, the ICP-OES results reveal that all the metals added during the synthesis processes are present in the catalysts. Besides, the BET surface areas of the catalysts are low (as correspond to solids with negligible porosity, as mixed oxides with perovskite structure are [11]) and they range from 5 to 13 m^2/g.

Table 1. Nomenclature and basic characterization data.

Catalyst	Nomenclature	S_{BET} (m^2/g)	Bexp (wt%)/ Bnom (wt%)	B/Ba+Ti+B [1]	$O_{lattice}$/Ba+Ti+B [2]
$BaTi_{0.8}Mn_{0.2}O_3$	BTMnO_2	13	5.2/5.4	0.08	1.5
$BaTi_{0.8}Fe_{0.2}O_3$	BTFeO_2	7	4.7/4.8	0.09	1.8
$BaTi_{0.8}Co_{0.2}O_3$	BTCoO_2	5	4.9/4.9	0.13	1.4
$BaTi_{0.8}Cu_{0.2}O_3$	BTCuO_2	12	4.9/5.0	0.07	1.4
$BaTiO_3$	BTO_ref	9	–	–	2.0

[1] B/Ba+Ti+B nominal = 0.1, [2] $O_{lattice}$/Ba+Ti+B nominal = 1.5.

Concerning the XRD results, Figure 1a shows the XRD patterns of the catalysts that reveal a perovskite like structure (the diffraction peaks observed at 2θ: 22.3°; 31.4°; 38.8°; 45.2°; 51.0°; 56.1°; 65.8°; 74.9°; for (100), (110), (111), (200), (210), (211), (220), and (310) lattice planes, correspond to the standard JCPDS for tetragonal perovskite structure: 5-626 [17]) as the major crystalline phase for all the catalysts. Based on the splitting of peak around 51°, it seems that the perovskite structure is tetragonal for BTO_ref and BTCuO_2, but it changes to cubic for the other catalysts [11,12]. The magnification of the main peak of the diffractograms (31.5°), included in Figure 1b, clearly shows a shift to a lower angle value, respect to the BTO reference which is more evident for BTMnO_2, BTCoO_2, and BTFeO_2 (suggesting a modification of the perovskite structure) [11,12] than for BTCuO_2 (as the tetragonal structure is preserved for this catalyst), even though a decrease in the peak intensity is featured. Additionally, other minority phases are also identified by XRD, that is, mainly Ba_2TiO_4 and $BaCO_3$ (formed by the carbonation of segregated barium oxide during samples atmospheric exposure) but also CuO for BTCuO_2, and only $BaCO_3$ for BTMnO_2, BTFeO_2, and BTCoO_2 catalysts. As it has been previously reported [11,12], the existence of segregated phases on a metal substituted

perovskite proves that the metal has been incorporated into the perovskite structure. Therefore, the shift of the main diffraction peaks ascribed to the perovskite structure and the segregation of minority phases identified in the XRD patterns indicate that Ti is successfully substituted by Mn, Fe, Co, and Cu in the perovskite framework. It is worth mentioning that: i) for BTCoO_2 catalysts, other cobalt phases ($BaCoO_3$ perovskite and Co_3O_4) are also identified as minority segregated phases in the XRD diffractogram, suggesting that cobalt has been introduced into the perovskite lattice in a lower extent than Cu, Fe, and Mn; and ii) Ba_2TiO_4, which has been suggested as an active phase for NOx storage [11,12], is only detected for BTCuO_2 catalyst.

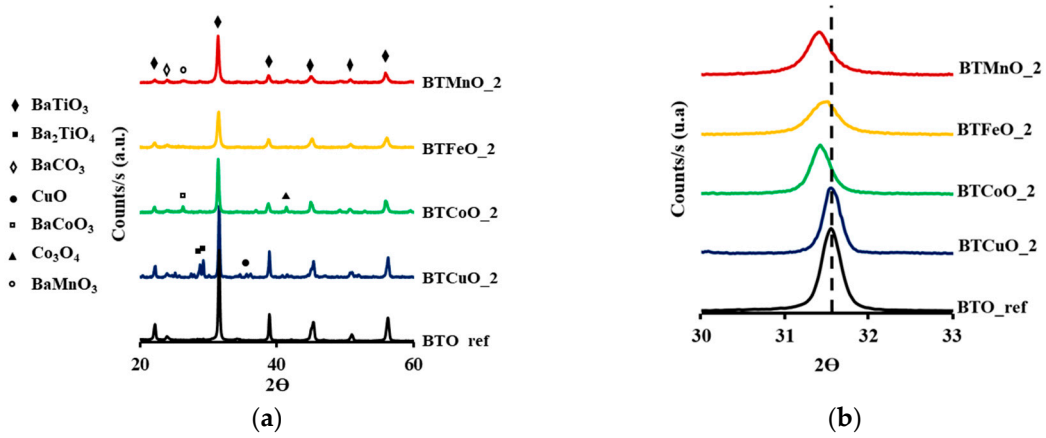

Figure 1. Catalysts characterization: (**a**) XRD patterns, (**b**) main peak magnification.

To verify the structural modifications in the perovskites suggested by XRD patterns, Raman spectroscopy was used. According to literature [18,19], only the tetragonal structure of $BaTiO_3$ perovskite, which belongs to space group P4mm, presents first-order Raman-active modes with bands at, approximately, 180 cm^{-1}, 265 cm^{-1}, 305 cm^{-1}, 520 cm^{-1}, and 720 cm^{-1}, corresponding to irreducible representations ((A1(LO)), (A1(TO)), (B1), (A1, E(TO)), and (A1, E(LO)), respectively. On the one hand, the Raman spectra, shown in Figure 2, confirm that BTCuO_2 preserves the original tetragonal structure of the raw perovskite, as suggested by XRD, as it features the main bands previously indicated. In spite of this, BTCuO_2 spectrum shows broader peaks than BTO spectrum, pointing out that copper incorporation distorts the original tetragonal structure. On the other hand, BTFeO_2 and BTMnO_2 catalysts show an almost flat spectrum, ascribed to perovskite cubic structure, which does not show active modes in Raman spectroscopy. Finally, some Raman peaks are identified in the BTCoO_2 spectrum which are ascribed to the presence of minority phases such as $BaCoO_3$ and Co_3O_4, also identified by XRD. This result supports that a lower degree of cobalt is incorporated into the perovskite framework of the catalyst.

The different effects of the B cations, that partially substitute Ti on the perovskite structure, seem to be related with their ionic radius. Fe, Mn, and Cu (as M^{2+}) have ionic radii larger than Ti^{4+} causing the distortion of the raw tetragonal perovskite structure. As Co^{2+} presents the most similar ionic radius to Ti^{4+}, the formation of the stable $BaCoO_3$ perovskite is also allowed and, consequently, a lower fraction of cobalt is inserted into the $BaTiO_3$ perovskite framework to partially replace titanium.

XPS provides valuable information about the catalysts surface composition. All the XPS spectra and contributions assignment are featured in Figure A1 and Table A1, in the Appendix A. Table 1 shows the data related to metal (Mn, Fe, Co, or Cu) distribution presented as B/Ba+Ti+B (B= Mn, Fe, Co, Cu) ratio, whilst the data related to lattice oxygen, is shown as $O_{lattice}$/Ba+Ti+B (B= Mn, Fe, Co, Cu) ratio. It can be observed that for Mn, Fe, and Cu, the B/Ba+Ti+B XPS ratio is lower than the corresponding nominal value (0.1), which supports that these metals have been partially introduced into the perovskite structure. The BTCuO_2 catalyst presents the lowest value, so, the highest percentage of metal inside the perovskite lattice, whilst for Co, a B/Ba+Ti+B ratio higher than the nominal is found due to the

presence of $BaCoO_3$ and Co_3O_4 segregated phases. The $O_{lattice}$/Ba+Ti+B XPS ratio (calculated from the area for O1s peak corresponding to lattice oxygen) for all catalysts is lower than the corresponding value for the BTO_ref perovskite (2.0), evidencing the creation of oxygen vacancies in the perovskite structure to compensate the imbalance in positive charge due to the partial substitution of Ti^{4+}. Note that the BTCuO_2 catalyst presents the lowest $O_{lattice}$/Ba+Ti+B ratio and, consequently, the largest amount of surface oxygen vacancies. This result seems to be explained considering that BTCuO_2 catalyst presents a positive imbalance larger than the other catalysts due to the highest difference between the oxidation state of Ti^{4+} and the Cu^{+2} (Fe and Mn appear mainly as Fe(II) and Mn(III) but Fe(III) and Mn(IV) have been also identified by XPS). Additionally, surface oxygen vacancies are also created because Ti^{+4} cannot achieve a higher oxidation state as other B cations (as Mn or Fe in $BaMn_{1-x}Cu_xO_3$ and $BaFe_{1-x}Cu_xO_3$ [20,21]) do. Finally, it is remarkable that BTCuO_2 catalyst preserves the original tetragonal structure (shown by XRD and Raman results), but with a high degree of distortion, which causes the presence of a larger amount of oxygen vacancies.

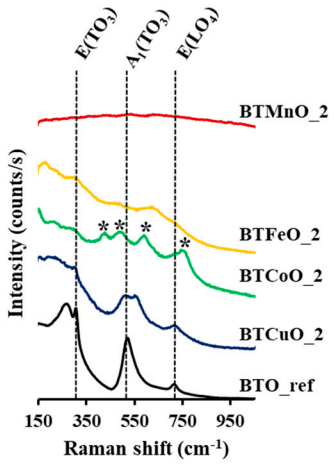

Figure 2. Catalysts characterization: Raman spectra.

2.2. Catalytic Activity

For the analysis of the activity of the catalysts for NO to NO_2 oxidation and NOx adsorption/desorption, temperature programmed reaction (TPR-NOx) experiments were carried out. These experiments also allow the selection of the optimal temperature for isothermal NOx storage experiments that have been carried out in order to determine the NOx storage capacity (NSC, which is the amount of NOx stored (in μmol) per gram of catalyst). The results obtained as explained in the Materials and Methods section are presented in Figure 3.

Figure 3a features the NOx conversion profiles for all catalysts. It has been considered that positive values of NOx% conversion indicate that NOx adsorption is taking place, while negative values correspond to a NOx desorption process. According to this, at temperatures lower than 500 °C, approximately, the NOx conversion profiles represent NOx adsorption profiles and, at temperatures higher than 500 °C, these represent NOx desorption profiles. An analysis of the NOx conversion profiles reveals that BTCoO_2 but, mainly, BTCuO_2 catalysts show NOx adsorption/desorption activity, this performance being consistent with the presence of Ba_2TiO_4 segregated phase, which has been suggested as an active phase for NOx adsorption [11,12].

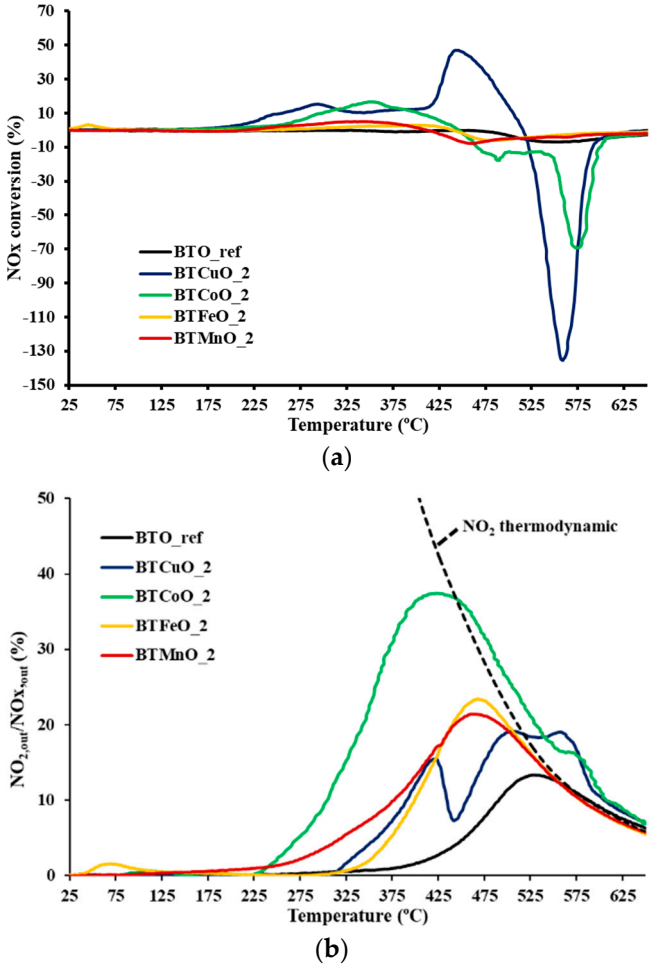

Figure 3. (**a**) NOx conversion profiles and (**b**) NO_2 generation profiles during the TPR-NOx experiments.

Before analyzing the NO_2 generation profiles shown in Figure 3b, it is worth mentioning that NO_2 is the main compound involved in NOx adsorption processes [8,11,12] and, for this reason, it has to be considered that the NO_2 registered by the analyzers is only the evolved NO_2, that is: i) below 500 °C, it is the fraction of NO_2 generated which is not stored; and ii) above 500 °C, it represents the NO_2 that is being desorbed. Therefore, the NO_2 generation shown in Figure 3b cannot be considered as a straight representation of the total NO_2 generated and, consequently, any conclusion regarding NO to NO_2 oxidation activity of the catalysts must be drawn from the combination of Figure 3a,b.

Thus, all the $BaTi_{0.8}B_{0.2}O_3$ perovskite catalysts increase the rate of NO_2 generation percentage at low temperature as the %NO_2 generated is higher than that shown by the BTO perovskite used as a reference (BTO_ref in Figure 3a,b). However, a deeper analysis of the data reveals some significant differences in the NO_2 profiles of the catalysts. Firstly, BTFeO_2 and BTMnO_2 catalysts feature Gaussian-shape NO_2 generation profiles with maxima at around 470 °C. Considering that almost any significant NOx adsorption/desorption activity is observed for these catalysts, it can be suggested that they are mainly active for NO to NO_2 oxidation (however, NOx adsorption capacity cannot be totally ruled out due to the intrinsic characteristics of TPR experiment). Secondly, although BTCoO_2 catalyst presents a similar type of NO_2 generation profile, it shows the highest NO oxidation activity, which seems to be related to the presence of Co_3O_4, as metal oxides are active for the NO to NO_2 oxidation reaction [11,12,14–16]. In addition, the low intensity NOx conversion peaks observed for BTCoO_2 catalyst in Figure 3a, indicates a low NOx adsorption activity that, according to literature [14–16], could be due to the presence of minority segregated phases and oxygen vacancies. Finally, a different NO_2 generation profile with two maxima and a minimum (at ca. 421, 507, and 441 °C, respectively) are

clearly identified for BTCuO_2 catalyst. It is worth indicating that the temperature of the minimum NO_2 generation perfectly matches with the temperature of the maximum NOx conversion observed for this catalyst in Figure 3a. This result points out that, at this temperature, BTCuO_2 shows higher NOx adsorption rate than NO oxidation rate as Ba_2TiO_4 phase, which is active for NOx adsorption [11,12], has been identified.

As a summary, TPR- NOx results reveal that only BTCuO_2 presents the NOx conversion and NO_2 generation profiles expected for LNT catalysts [11,12]. Thus, even though all the catalysts present active sites for NO-to-NO_2 oxidation, such as oxygen vacancies and surface metal oxides, only the catalyst containing copper shows the presence of the Ba_2TiO_4 segregated phase, which is active for NOx adsorption [11,12].

In order to determine the NSC, NOx storage experiments at 400 °C (the minimum temperature for NOx adsorption in TPR-NOx profiles) have been carry out for the three perovskites in which Ti has been substituted in a larger degree, that is, BTCuO_2, BTFeO_2, and BTMnO_2. The NSC values (shown in Table 2) have been obtained during the 10th NOx storage cycle at which the catalysts achieve a stable performance (see Materials and Methods section for more details). Figure 4 shows, as an example, the NO, NO_2, and NOx profiles during NSC experiments at 400 °C, corresponding to the BTCuO_2 catalyst.

Table 2. NSC data at 400 °C for BTO reference, $BaTi_{0.8}B_{0.2}O_3$ catalysts and for some reference noble metal-base catalysts.

Catalyst	NSC (μmol/g)	Temperature (°C)	Lean Cycle Time (s)
BTMnO_2	83	400	300
BTFeO_2	99	400	300
BTCuO_2	269	400	300
1%Pt/20%BaO/Al_2O_3 [10]	150	350	120
2.2%Pt/16.3%BaO/Al_2O_3 [11]	400	350	240
2.2%Pt/20.8%BaO/Al_2O_3 [12]	240	300	240

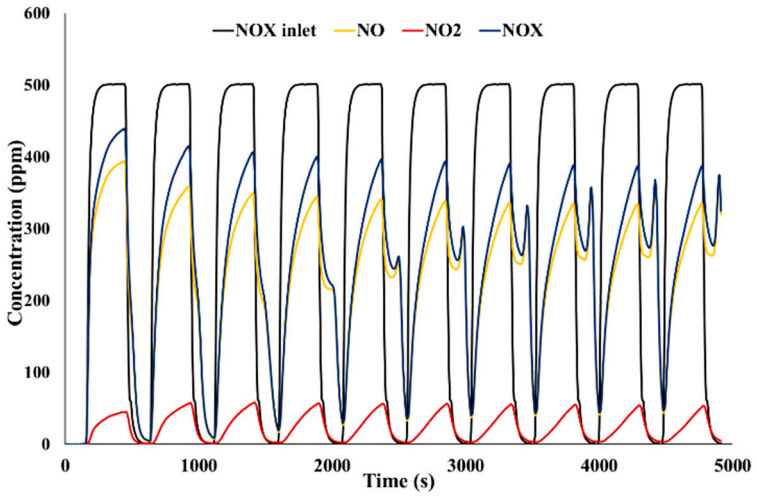

Figure 4. NSC cycles at 400 °C for the BTCuO_2 catalyst.

Data on Table 2 reveals that the three catalysts present a measurable NSC, but, in agreement with TPR-NOx results, BTCuO_2 catalyst is the most active one. The characterization results previously discussed allow us to justify the high NSC shown by copper perovskite. On the one hand, the incorporation of Cu into the perovskite lattice distorts the raw tetragonal structure, generates the largest pool of oxygen vacancies, and promotes the segregation of mainly Ba_2TiO_4 and $BaCO_3$, but also CuO as segregated phases that seem to be the active sites for both NO to NO_2 oxidation and NOx storage [11,12]. On the other hand, the insertion of Mn and Fe causes a structural change from

tetragonal to cubic, but only $BaCO_3$ appears as segregated phase and a lower amount of oxygen vacancies respect to Cu. Consequently, a lower NO to NO_2 oxidation activity and NSC is shown by these two catalysts. Finally, it is important to underline that the NSC of BTCuO_2 is within the range of values reported for noble metal/alkali or alkali earth base catalysts (Table 2). Moreover, the BTCuO_2 perovskite does not incorporate any noble metal, and therefore it could be a cheaper alternative to current catalysts based on noble metals. Additionally, as this catalyst works at 400 °C, presenting an acceptable NOx storage capacity, it could be proposed as a component of high-temperature LNT for lean burn gasoline engines (GDI gasoline direct injection) which need catalysts working between 400 and 500 °C.

3. Materials and Methods

Four $BaTi_{0.8}B_{0.2}O_3$ catalysts (being B Mn, Fe, Co, or Cu), named BTMnO_2, BTFeO_2, BTCoO_2, and BTCuO_2 respectively, were prepared by the sol–gel method as previously described [11]. Summarizing, first of all, the hydrolysis of titanium isopropoxide (Ti) was carried out, dissolving the resulting species in an aqueous solution of citric acid (CA) (Ti:CA = 1:2) and hydrogen peroxide ($Ti:H_2O_2$ = 2:1), and obtaining the citrate–peroxo–titanate (IV) complex. Subsequently, NH_3 was used in order to adjust the pH to 8.5, and the addition of an stoichiometric ($BaTi_{0.8}B_{0.2}O_3$) amount of barium (Ba:Ti = 1:1) and metals precursors (barium acetate and Fe, Co, Cu, and Ni nitrates), took place. During 5 h, until the obtention of a gel, the temperature of the mixture remained 65 °C. Afterwards, a temperature of 90 °C or 24 h was used to dry the sample, which was in the end calcined at 850 °C for 6 h.

To measure the metal content in the samples by ICP-OES, a Perkin-Elmer device model Optima 4300 DV was used. An Autosorb-6B instrument from Quantachrome served to determine, by N_2 adsorption at −196 °C, the BET surface area of the samples. To identify different phases and crystalline structures, X-ray diffraction (XRD) and Raman spectroscopy were employed. XRD tests were performed with a Rigaku Miniflex II powder diffractometer, using Cu Kα (0,15418 nm) radiation with the 2θ angle in the range 20 to 80°, with a step of 0.025° and a time per step of 2 s. Raman scattering spectra were obtained on a Jobin-Ivon dispersive Raman spectrometer (model LabRam) with a variable power He:Ne laser source (633 nm) in the range of 100–1000 nm. To register the XPS spectra, a K-Alpha photoelectron spectrometer by Thermo-Scientific, with an Al Kα (1486.6 eV) radiation source, was used in the following conditions: 5×10^{-10} mbar pressure in the chamber and setting the C1s transition at 284.6 eV, and the binding energy (BE) and kinetic energy (KE) values then determined with the peak-fit software of the spectrophotometer, to regulate the BE and KE scales.

The catalytic activity of the samples (80 mg of catalyst diluted in 300 mg SiC) was tested using two different experiments in a fixed-bed quartz reactor at atmospheric pressure and under a gas flow (500 mL/min): i) temperature programmed reaction (TPR-NOx) tests (10 °C/min, 800 °C) in a gas mixture of 500 ppm NOx and 5 % O_2 and ii) NOx storage cyclic tests at 400 °C, with a gas mixture composed of: i) for lean (storage) cycle (5 min), 500 ppm NOx and 5 % O_2 balanced with N_2, and ii) for rich (regeneration) cycle (3 min), 10% H_2 balanced with N_2. To achieve the stability of the catalysts, and then determine the NSC, 10 consecutive storage–regeneration cycles were accomplished. The gas composition was controlled by specific NDIR-UV gas analyzers for NO, NO_2, CO, CO_2, and O_2 (Rosemount Analytical Model BINOS 1001, 1004, and 100).

NOx conversion profiles as a function of temperature were obtained using the next equation

$$\text{NOx conversion } (\%) = \frac{NOx_{in} - NOx_{out}}{NOx_{in}} \times 100$$

where 'NOx_{in}' is the concentration of NOx (=NO + NO_2) feed to the reactor and 'NOx_{out}' is the concentration of NOx that leaves the reactor.

The percentage of NO_2 generated during TPR was determined with the equation

$$NO_2(\%) = \frac{NO_{2,out}}{NO_{2,in}} \times 100$$

where 'NO_{2out}' is the concentration of NO_2 that leaves the reactor.

The NSC was obtained as the difference between the NOx signal when the reactor is unfilled and the NOx signal when the reactor is full of catalyst with

$$\text{NOx storage} = \int_{t0}^{tf} NOx_{inlet}(t) - NOx_{exp}(t)dt$$

where 'NOx_{inlet}' is the concentration of NOx (=NO + NO_2) measured when the reactor is empty, and 'NOx_{exp}' is the concentration of NOx during the NOx storage test.

4. Conclusions

From the analysis of the effect of Ti partial substitution by Mn, Fe, Co, or Cu on the NOx storage capacity (NSC) of the $BaTi_{0.8}B_{0.2}O_3$ lean NOx trap (LNT) catalyst, the following conclusions have been obtained:

- In $BaTi_{0.8}B_{0.2}O_3$ perovskites, Ti is partially substituted by Mn, Fe, Cu and, to a lower extent, by Co.
- The perovskite structure is modified or changed due to the insertion of B metal into the lattice:
    - (i) For the BTCuO_2 catalyst, the tetragonal structure of the raw perovskite is distorted, a larger amount of oxygen vacancies is generated and Ba_2TiO_4 and $BaCO_3$ appear as main minority segregated phases, but CuO is also detected.
    - (ii) For Mn, Fe, and Co, the tetragonal structure changes to cubic, a lower amount of oxygen vacancies are formed and $BaCO_3$ appears as segregated phase in the three catalysts. BTCoO_2 presents also $BaCoO_3$ and Co_3O_4 segregated phases due to a lower degree of Co insertion into the framework.
- Due to the described modifications, all the $BaTi_{0.8}B_{0.2}O_3$ catalysts are active for the NO oxidation to NO_2, which takes place on oxygen vacancies and metal oxide sites, but only the BTCuO_2 catalyst (for which Ba_2TiO_4 segregated phase is identified), presents a significant NOx storage capacity. In fact, at 400 °C, the BTCuO_2 catalyst features the highest NSC which is close to that shown by platinum base catalysts.

Author Contributions: Conceptualization, V.A.-F. and M.-J.I.-G.; Methodology, V.A.-F. and M.-J.I.-G.; Validation, V.A.-F, M.-S.S.-A., and M.-J.I.-G.; Formal analysis, C.A., V.T.-R., V.A.-F, M.-S.S.-A., and M.-J.I.-G.; Investigation, C.A., V.T.-R., V.A.-F.; Resources, M.-S.S.-A. and M.-J.I.-G.; Data curation, V.A.-F., M.-S.S.-A. and M.-J.I.-G.; Writing—original draft preparation, C.A., V.T.-R., and V.A.-F; Writing—review and editing, M.-S.S.-A. and M.-J.I.-G.; Visualization, C.A., V.A.-F., and M.-S.S.-A.; Supervision, V.A.-F. and M.-J.I.-G; Project administration, M.-J.I.-G.; Funding acquisition, M.-S.S.-A. and M.-J.I.-G.

Funding: This research was funded by Generalitat Valenciana (PROMETEO/2018/076 and Ph.D. grant ACIF 2017/221), Spanish Government (MINECO Project CTQ2015-64801-R) and EU (FEDER Founding).

Conflicts of Interest: The authors declare no conflict of interest.

Appendix A

Figure A1 shows the XPS spectra obtained for (a) BTCuO_2, (b) BTCoO_2, (c) BTFeO_2, and (d) BTMnO_2. Each figure contains the XPS spectra for the substituted metal ($Cu2p^{3/2}$, Co2s, $Fe2p^{3/2}$, $Mn2p^{3/2}$ transitions), oxygen (O1s transition), and barium ($Ba3d^{5/2}$ transition). In the spectra, the red lines represent the normalized peak and the blue lines represent the deconvolution of the normalized peaks.

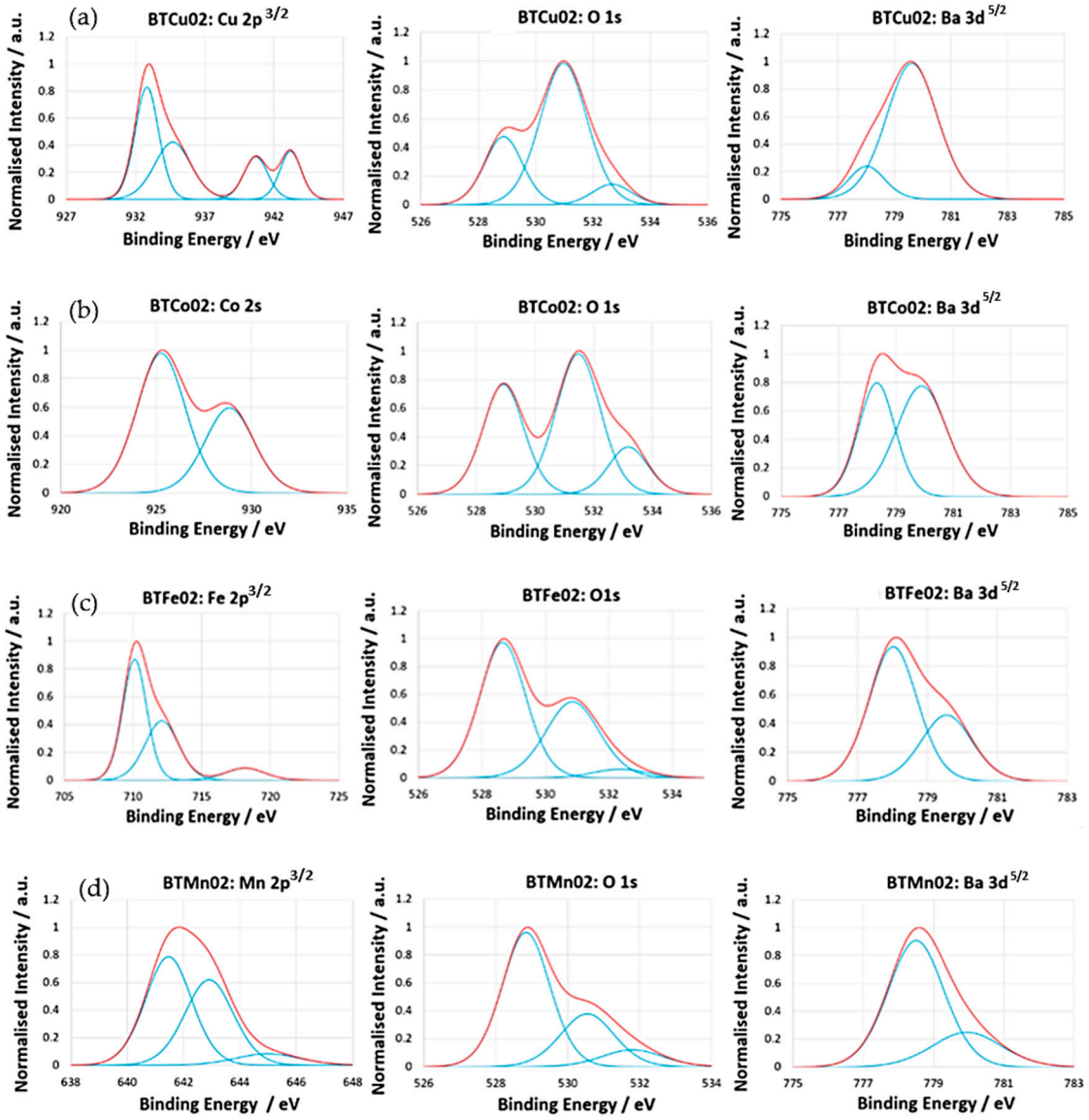

Figure A1. XPS spectra obtained for (**a**) BTCuO_2, (**b**) BTCoO_2, (**c**) BTFeO_2, and (**d**) BTMnO_2.

The XPS spectra of the O1s transition show three contributions for all the catalysts that, according to literature [22,23], can be ascribed to: (i) lattice oxygen of metal oxides at ca. 529 eV; (ii) surface oxygen species such as oxygen peroxides (O_2^{2-}), surface carbonates (CO_3^{2-}), and/or hydroxyl groups (OH^-), at ca. 531 eV; and (iii) adsorbed water at ca. 533 eV.

The XPS spectra of the $Ba3d^{5/2}$ transition for all the catalysts show two contributions at approximately 778 eV and 780 eV binding energies. According to literature [24], they can be ascribed to: (i) Ba(II) oxide species ($BaCuO_2$, $BaTiO_3$-tet., Ba_2TiO_4), and (ii) $BaCO_3$ respectively.

The assignment of the different contributions found in the XPS spectra of the substituted metal ($Cu2p^{3/2}$, Co2s, $Fe2p^{3/2}$, $Mn2p^{3/2}$) transitions is shown in Table A1.

Table A1. Binding energy and assignment of the Cu2p, Co2s, Fe2p, and Mn2p transitions.

XPS Transition	Binding Energy (eV)	Assigned Species
$Cu2p^{3/2}$	932.9	Cu(II) oxide surface species [25,26]
	934.8	Lattice Cu(II) [11]
	940.8	Cu(II) satellite [25]
	943.3	Cu(II) satellite [25]
Co2s	925.28	Co (II) oxide species [24]
	928.88	Co(III) oxide species (Co_3O_4)
$Fe2p^{3/2}$	710.12	Fe(II) oxide species [24]
	712.09	Fe (III) oxide species [24]
	718.15	Fe (III) Satellite [25]
$Mn2p^{3/2}$	641.46	Mn(III) oxide species ($BaMn_8O_{16}$) [27]
	642.90	Mn(IV) oxide species ($BaMn_8O_{16}$, $BaMnO_{3-x}$) [27]
	644.98	Mn satellite [26,28]

References

1. Hasan, A.O.; Abu-jrai, A.; Turner, D.; Tsolakis, A.; Xu, H.M.; Golunski, S.E.; Herreros, J.M. Control of harmful hydrocarbon species in the exhaust of modern advanced GDI engines. *Atmos. Environ.* **2016**, *129*, 210–217. [CrossRef]
2. Polat, S.; Uyumaz, A.; Solmaz, H.; Yilmaz, E.; Topgül, T.; Yücesu, H.S. A numerical study on the effects of EGR and spark timing to combustion characteristics and NOx emission of a GDI engine. *Int. J. Green Energy* **2016**, *13*, 63–70. [CrossRef]
3. Epling, W.; Nova, I.; Szanyi, J.; Yezerets, A. Diesel emissions control catalysis. *Catal. Today* **2010**, *151*, 201. [CrossRef]
4. Breen, J.P.; Marella, M.; Pistarino, C.; Ross, J.R.H. Sulfur-Tolerant NOx Storage Traps: An Infrared and Thermodynamic Study of the Reactions of Alkali and Alkaline-Earth Metal Sulfates. *Catal. Lett.* **2002**, *80*, 123–128. [CrossRef]
5. Gill, L.J.; Blakeman, P.G.; Twigg, M.V.; Walker, A.P. The Use of NOx Adsorber Catalysts on Diesel Engines. *Top. Catal.* **2004**, *28*, 157–164. [CrossRef]
6. Pereda-Ayo, B.; González-Velasco, J.R. NOx Storage and Reduction for Diesel Engine Exhaust Aftertreatment. In *Diesel Engine—Combustion Emissions and Condition Monitoring*; Bari, S., Ed.; IntechOpen Ltd.: London, UK, 2013; pp. 161–196. ISBN 978-953-51-1120-7.
7. Bowker, M. Automotive catalysis studied by surface science. *Chem. Soc. Rev.* **2008**, *37*, 2204–2211. [CrossRef] [PubMed]
8. Epling, W.S.; Campell, L.E.; Currier, N.W.; Parks, J.E. Overview of the Fundamental Reactions and Degradation Mechanisms of NOx Storage/Reduction Catalysts. *Catal. Rev. Sci. Eng.* **2004**, *46*, 163–245. [CrossRef]
9. Ad Hoc Working Group on Defining Critical Raw Materials. *Report on Critical Raw Materials for the EU*. 26 May 2014. Available online: http://www.catalysiscluster.eu/wp/wp-content/uploads/2015/05/2014_Critical-raw-materials-for-the-EU-2014.pdf (accessed on 15 January 2019).
10. Royer, S.; Duprez, D.; Can, F.; Courtois, X.; Batiot-Dupeyrat, C.; Laassiri, S.; Aalmdari, H. Perovskites as Substitutes of Noble Metals for Heterogeneous Catalysis: Dream or Reality. *Chem. Rev.* **2014**, *114*, 10292–10368. [CrossRef]
11. Albaladejo-Fuentes, V.; López-Suárez, F.E.; Sánchez-Adsuar, M.S.; Illán-Gómez, M.J. $BaTi_{1-x}Cu_xO_3$ perovskites: The effect of copper content in the properties and in the NOx storage capacity. *Appl. Catal. A Gen.* **2014**, *488*, 189–199. [CrossRef]
12. Albaladejo-Fuentes, V.; López-Suárez, F.E.; Sánchez-Adsuar, M.S.; Illán-Gómez, M.J. Tailoring the properties of $BaTi_{0.8}Cu_{0.2}O_3$ catalyst selecting the synthesis method. *Appl. Catal. A Gen.* **2016**, *519*, 7–15. [CrossRef]
13. Modeshia, D.R.; Walton, R.I. Solvothermal synthesis of perovskites and pyrochlores: Crystallisation of functional oxides under mild conditions. *Chem. Soc. Rev.* **2010**, *39*, 4303–4325. [CrossRef]

14. Wang, J.; Su, Y.; Wang, X.; Chen, J.; Zhao, Z.; Shen, M. The effect of partial substitution of Co in $LaMnO_3$ synthesized by sol–gel methods for NO oxidation. *Catal. Commun.* **2012**, *25*, 106–109. [CrossRef]
15. Dhal, G.C.; Dey, S.; Mohan, D.; Prasad, R. Study of Fe, Co, and Mn-based perovskite-type catalysts for the simultaneous control of soot and NOX from diesel engine exhaust. *Mater. Discov.* **2017**, *10*, 37–42. [CrossRef]
16. Li, Z.; Meng, M.; Zha, Y.; Dai, F.; Zhang, J. Highly efficient multifunctional dually-substituted perovskite catalysts $La_{1-x}K_xCo_{1-y}Cu_yO_{3-\delta}$ used for soot combustion, NOx storage and simultaneous NOx-soot removal. *Appl. Catal. B Environ.* **2012**, *121–122*, 65–74. [CrossRef]
17. Xia, F.; Liu, J.; Gu, D.; Zhao, P.; Zhang, J.; Che, R. Microwave absorption enhancement and electron microscopy characterization of $BaTiO_3$ nano-torus. *Nanoscale* **2011**, *3*, 3860–3867. [CrossRef]
18. Hayashi, H.; Nakamura, T.; Ebina, T. In-situ Raman spectroscopy of $BaTiO_3$ particles for tetragonal–cubic transformation. *J. Phys. Chem. Solids* **2013**, *74*, 957–962. [CrossRef]
19. Asiaie, R.; Zhu, W.D.; Akbar, S.A.; Dutta, P.K. Characterization of Submicron Particles of Tetragonal $BaTiO_3$. *Chem. Mater.* **1996**, *8*, 226–234. [CrossRef]
20. Torregrosa-Rivero, V.; Albaladejo-Fuentes, V.; Sánchez-Adsuar, M.S.; Illán-Gómez, M.J. Copper doped $BaMnO_3$ perovskite catalysts for NO oxidation and NO_2-assisted diesel soot removal. *RSC Adv.* **2017**, *7*, 35228–35238. [CrossRef]
21. Moreno-Marcos, C.; Torregrosa-Rivero, V.; Albaladejo-Fuentes, V.; Sánchez-Adsuar, M.S.; Illán-Gómez, M.J. $BaFe_{1-x}Cu_xO_3$ Perovskites as Soot Oxidation Catalysts for Gasoline Particulate Filters (GPF): A Preliminary Study. *Top. Catal.* **2018**. [CrossRef]
22. Merino, N.A.; Barbero, B.P.; Eloy, P.; Cadus, L.E. $La_{1-x}Ca_xCoO_3$ perovskite-type oxides: Identification of surface oxygen species by XPS. *Appl. Surf. Sci* **2016**, *253*, 1489–1493. [CrossRef]
23. Ponce, S.; Peña, M.; Fierro, J.L. Surface properties and catalytic performance in methane combustion of Sr-substituted lanthanum manganites. *Appl. Catal. B Environ.* **2000**, *24*, 193–205. [CrossRef]
24. NIST X-ray Photoelectron Spectroscopy Database. (n.d.). Available online: https://srdata.nist.gov/xps/ (accessed on 15 January 2019).
25. XPS Simplified Knowledge Base. (n.d.). Available online: http://xpssimplified.com/knowledgebase.php (accessed on 15 January 2019).
26. Mingmei, W.; Qiang, S.; Gang, H.; Yufang, R.; Hongyiang, W. Preparation and Properties of $BaCuO_{2.5}$ and Its Related Oxides. *J. Solid State Chem.* **1994**, *110*, 389–392. [CrossRef]
27. Lan, L.; Li, Y.; Zeng, M.; Mao, M.; Ren, L.; Yang, Y.; Liu, H.; Yun, L.; Zhao, X. Efficient UV–vis-infrared light-driven catalytic abatement of benzene on amorphous manganese oxide supported on anatase TiO_2 nanosheet with dominant {001} facets promoted by a photothermocatalytic synergetic effect. *Appl. Catal. B Environ.* **2017**, *203*, 494–504. [CrossRef]
28. Liu, P.; He, H.; Wei, G.; Liu, D.; Liang, X.; Chen, T.; Zhu, J.; Zhu, R. An efficient catalyst of manganese supported on diatomite for toluene oxidation: Manganese species, catalytic performance, and structure-activity relationship. *Microporous Mesoporous Mater.* **2017**, *239*, 101–110. [CrossRef]